Microwave-Synthesized Tin Oxide Nanocrystals for Low-Temperature Solution-Processed Planar Junction Organo-Halide Perovskite Solar Cells

Journal of Materials Chemistry A

Accepted Manuscript

This article can be cited before page numbers have been issued, to do this please use: M. Abulikemu, M. Neophytou, J. Barbé, M. L. Tietze, A. El Labban, D. H. Anjum, A. Amassian, I. Mcculloch and S. Del Gobbo, *J. Mater. Chem. A*, 2017, DOI: 10.1039/C7TA00975E.

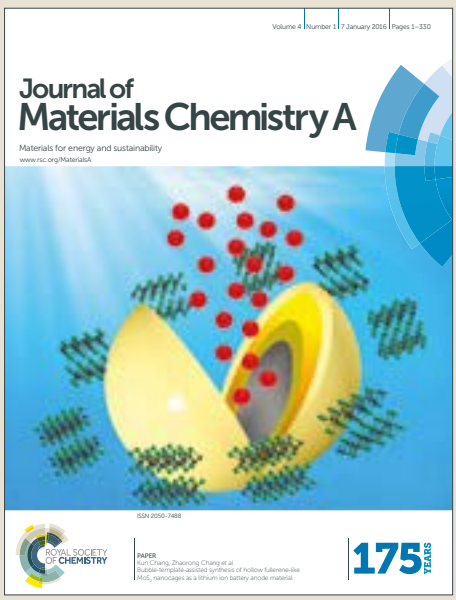

ROYAL SOCIETY OF CHEMISTRY

rsc.li/materials-a

View Article Online
DOI: 10.1039/C7TA00975E

Journal of Material Chemistry A

COMMUNICATION

Microwave-Synthesized Tin Oxide Nanocrystals for Low-Temperature Solution-Processed Planar Junction Organo-Halide Perovskite Solar Cells

How to bloReceived 00th January 20xx,
Accepted 00th January 20xx

DOI: 10.1039/x0xx00000x

www.rsc.org/

Mutalifu Abulikemu[1] Marios Neophytou[1], Jeremy M. Barbe[1,3], Max L. Tietze[1], Abdulrahman El Labban[1], Dalaver Anjum[1], Aram Amassian[1], Iain McCulloch[1], and Silvano Del Gobbo[1,2]*

Abstract. Tin oxide has been demonstrated to possess outstanding optoelectronic properties such as optical transparency and high electron mobility, therefore, it was successfully utilized as electron transporting layer in various kinds of solar cells. In this study, for the first time, highly dispersible SnO_2 nanoparticles were synthesized by microwave-assisted non-aqueous sol-gel route in an organic medium. Ethanol dispersion of the as-prepared nanoparticles was used to cast an uniform thin layer of SnO_2 without the aid of aggregating agent and at low temperatures. Organohalide perovskite solar cells were fabricated using SnO_2 as electron transporting layer. Morphological and spectroscopic investigations, in addition to the good photoconversion efficiency obtained, evidenced that nanoparticles synthesized by this route have optimal properties such as small size and crystallinity to form a continuous film. Furthermore, this method allows high reproducibility and scalability of the film deposition process.

Since the introduction of halide perovskite as photovoltaic light harvester by Miyasaka and co-workers in 2009[1], it has been received great attention from the solar energy community due its superior optical and electrical properties compared to other light harvesting materials. The power conversion efficiency of organo-halide perovskite based solar cells (OPSCs) rapidly reached 22.1%[2] in just 6 years of research, starting from initially only 3.8%.[1] This considerable improvement is not only based on optimization of halide perovskite preparation and casting methods, but also includes the proper choice of charge transporting layers which are crucial for device efficiency. In that regard, TiO_2, ZnO, SnO_2, Zn_2SnO_4, CdS and CdSe have been successfully used as electron transport materials (ETM).[3–10] Besides, a large variety of inorganic and organic materials have been used as hole transporting materials (HTM),[11–19] although, most of them are employed in inverted configuration OPSCs. Among all ETMs, compact and/or mesoporous TiO_2 are the most widely used and experimentally mature ETMs since TiO_2 was initially developed for dye sensitized solar cells (DSSC)[20] and afterwards naturally transferred to organo-halide perovskite solar cells.[1,3,4] However, TiO_2 thin films usually require thermal annealing at 500 – 600 °C for high quality film formation, resulting in increased costs and fabrication time. Besides, high temperatures are not compatible with every kind of substrates, in particular, not with polymeric flexible substrates. Therefore, low-temperature solution processed TiO_2 nanoparticle (NP) films were suggested as excellent alternative to TiO_2 films fabricated by traditional high temperature methods.[8,21] Although TiO_2 is widely used in the most efficient

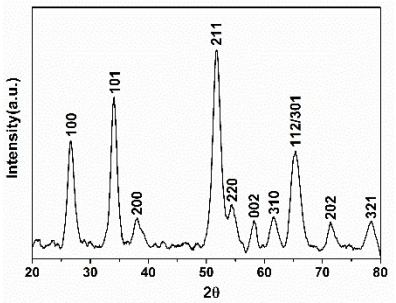

Figure 1: Powder XRD pattern of SnO_2-NPs grown for 1.5 h. On each peak are reported the Miller's indexes (hkl) identifying the specific reflection.

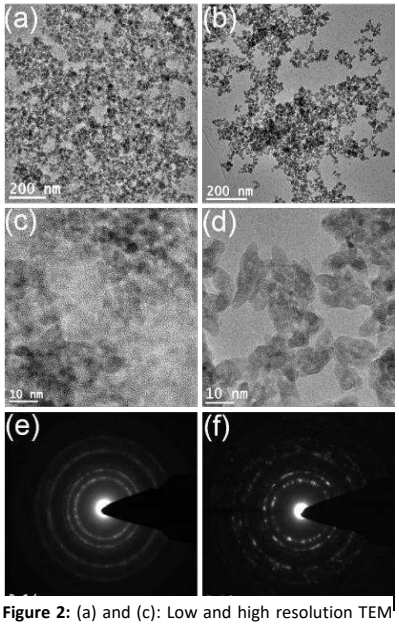

Figure 2: (a) and (c): Low and high resolution TEM images of small SnO_2-NCs (1.5 h growth time). (b) and (d): Low and high resolution TEM images of larger NCs (5 h growth time). (e) and (f): SAED pattern of the small and large SnO_2-NCs.

[a] KAUST Solar Center (KSC), King Abdullah University of Science and Technology (KAUST), 23955-6900 Thuwal, Saudi Arabia.
[b] School of Molecular Science and Engineering, Vidyasirimedhi Institute of Science and Technology, 555 Moo 1, Payupnai, Wangchan, Rayong, Thailand.
[c] 3- SPECIFIC – Swansea University College of Engineering, Bay Campus, Swansea SA1 8EN, UK

Electronic Supplementary Information (ESI) available: [details of any supplementary information available should be included here]. See DOI: 10.1039/x0xx00000x

perovskite solar cells, SnO_2 possesses a higher conductivity and electron mobility[22], which can enhance current density of OPSCs and increase charge collection at the anode, respectively. Also, thanks to its larger band-gap, SnO_2 decreases parasitic absorption caused by the ETL. Moreover, the favourable energy level alignment at the SnO_2/perovskite interface can facilitate photo-generated electrons injection from the halide perovskite to the SnO_2.[23–27] Furthermore, SnO_2, thanks to a wider band-gap, is more stable under UV light

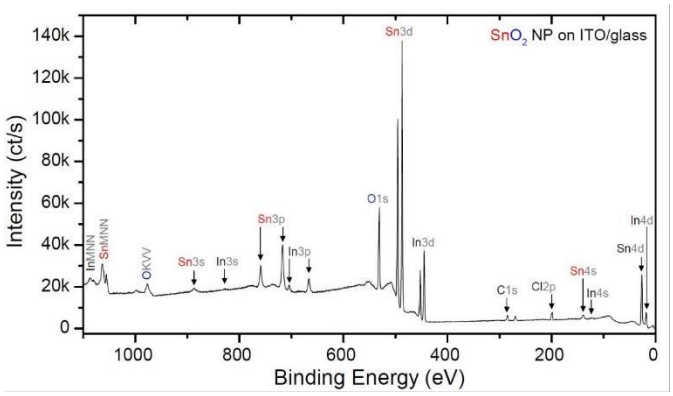

Figure 4: XPS survey scan of a SnO2 nanoparticle film obtained from 1.5 h synthesis. High-resolution peak scans of Sn3d (b) and O1s (c).

illumination compared to TiO_2 and ZnO.[22] All these aspects make SnO_2 theoretically preferable ETM over TiO_2 for OPSCs. Recently, Ke et al. reported that SnO_2 can be used as efficient ETM in OPSCs, in which SnO_2 was spin-coated from a precursor solution and subsequently annealed at 180°C.[23] In another report, high quality SnO_2 prepared by atomic layer deposition (ALD) was used as ETM yielding over 18% device efficiency.[27] More recently, Rao et al. demonstrated a device based on SnO_2 nanocolloids grown at room temperature, but corresponding devices reached only 6.52 % efficiency.[25] However, the efficiency was more than doubled (>14%) when the resulting SnO_2 film was coated with a thin layer of TiO_2 through impregnation with $TiCl_4$ followed by annealing at 520°C.[25] Besides the quoted reports, differently from TiO_2 there is only one low-temperature processed SnO_2-NCs-based ETLs for OPSCs, where, however, commercial SnO_2-NPs were used and the light absorber was $HC(NH_2)_2PbI_3$.[28] Therefore, due to the advantages of SnO_2

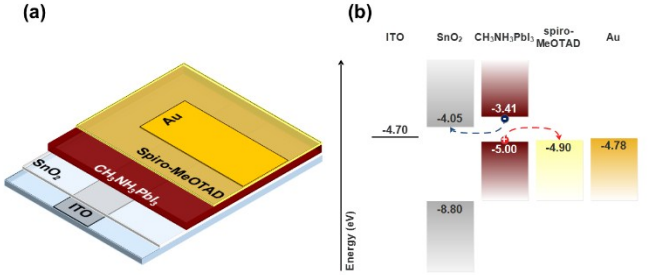

Figure 5: (a) Schematic view of the solar cell structure. (b) Energy band diagram of the perovskite solar cell, showing the separation and collection of photogenerated electrons and holes. The energy values of the SnO2-NCs film were obtained from the combination of UPS and optical absorption measurements, while for the other materials literature values are used.

mentioned above, we expect that SnO_2 NCs-based ETL could actually outperform the TiO_2-NCs reference cell although no binding/compacting additives (e.g. titanium diisopropoxide bis(acetylacetonate), $TiCl_4$) are used.[8,21,29] Herein, we present a low-temperature synthesis of SnO_2-NCs with controllable size and its application in OPSCs as a precursor for ETL. To prepare SnO_2-NCs, microwave assisted non-aqueous sol-gel (MW-NASG) synthesis is employed. SnO_2-NCs were already obtained through a similar route by Ba et al.[30], yet, we introduce the use of microwaves to initiate and sustain the reaction. Heating by microwave irradiation has been demonstrated to reduce the reaction time over conventional non-aqueous sol-gel synthesis and allows a more precise control of the reaction parameters such as the temperature, pressure and reaction time, all in favor of a higher yield and reproducibility.[31,32] In a typical SnO_2-NCs synthesis, 0.85 ml $SnCl_4$, 3 ml ethanol and 17 ml benzyl alcohol were mixed into 20 ml microwave vial inside a glove box. After sealing with a headspace cap, the vial was transferred to a microwave reactor cavity, and the reaction was carried out at 130°C for two different reaction times (1.5 and 5 hours) to observe its effect on the NCs size. Once the reaction is completed, the final product was washed three times by centrifugation, alternating dispersion in ethanol and precipitation with diethyl-ether before the precipitate was dried under vacuum. Finally, the powder of as-synthesized NCs was dispersed in ethanol. Several control experiments indicated that at least 90 minutes of microwave driven reaction are needed for formation of SnO_2-NCs, which is further indicated by a turning of the solution from transparent to milky. The obtained product is first characterized by powder X-ray diffraction (PXRD) and transmission electron microscopy (TEM). The XRD pattern in Figure 1 shows that the as-prepared NCs are crystalline and that no secondary phases are formed. A rough estimation of NCs sizes by Debye-Scherrer formula provides an average diameter of 6.3 nm. TEM and high resolution (HR) TEM micrographs (Figure 2a and c) show that the particles grown for 1.5 h possess a mildly irregular spherical shape with an average size of approximately 3 nm. The discrepancy between the size obtained from TEM micrographs and XRD can be explained by the formation of larger crystallographically coherent domains made up of NCs. The selected area electron diffraction (SAED) pattern (Figure 2e) confirms that the colloids are highly crystalline. It is further observed that the NCs size can be controlled by adjusting the reaction time. When the reaction was run for 5 hours under identical conditions of temperature and concentration, oblong irregular particles with an average size of 10 nm are obtained (Figure 2b and d). As for the smaller NCs, the single nanoparticle diffraction pattern of Figure 2f evidences the high crystallinity of the larger particles. Ultraviolet photoelectron spectroscopy (UPS) and X-ray photoelectron spectroscopy (XPS) are carried out to gain information about the band structure and composition of the SnO_2 NCs thin film, respectively. UPS (Figure S1) shows that the work function (WF) of as-synthesized SnO_2-NCs is 4.71 eV, which is significantly higher than that of TiO_2-NCs.[3,4] The ionization energy, obtained as the sum of the valence band onset and WF, is determined to be 8.80 eV, which is slightly higher than that of amorphous SnO_2 prepared by chemical bath deposition.[33] An XPS survey scan (cf. Figure 3) reveals that the film mostly contains oxygen (O1s) and Sn as expected for SnO_2. However, the spectrum also

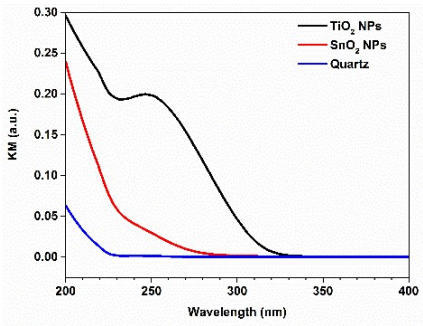

Figure 3: Kubelka-Munk graphs of SnO_2 and TiO_2-NCs thin films deposited on quartz substrates measured by diffuse reflectance spectroscopy (integrating sphere). For comparison, the Kubelka-Munk function of the bare quartz substrate is given (blue line).

contains noticeable signal originating from indium, i.e., from the ITO substrate underneath, which indicates that the formed SnO_2-NP film is either thinner than the free mean path of the photoelectrons or that it may contain pinholes. Furthermore, a relatively weak signal attributable to chlorine is detected (cf. Figure 3, Cl2p peak). We assume that it residues comes from the used $SnCl_4$ precursor used for the synthesis. As-synthesized SnO_2-NCs are dispersed in ethanol, and the NCs dispersion is spin-coated on cleaned ITO/glass substrates immediately after UV-O_3 treatment. Then, in sequence, $MAPbI_3$ and Spiro-MeOTAD are deposited on the SnO_2 ETL layer. The detailed materials preparation, device fabrication processes and characterizations are described more in details in the supporting information. The device architecture and corresponding energy levels are illustrated in Figure 4a and b, respectively. Furthermore, TiO_2-NCs of similar size like the sub-5 nm SnO_2-NCs were synthesized by the same method to compare the optical properties and effectiveness as ETM of both materials. Kubelka-Munk spectra (Figure 5) indicate an absorption onset starting at much lower wavelengths for SnO_2-NCs as compared to TiO_2-NCs. It suggests that by replacing TiO_2 with SnO_2, one can decrease parasitic absorption within the ETL and, thus, increase the current density of the final device. The band-gap of the SnO_2-NCs thin film was determined from Tauc plot extrapolation to be 4.75 eV (Figure S2). This value is far higher than the band-gap of bulk SnO_2 (E_g = 3.6 eV)[34] indicating a strong quantum confinement effect due to the reduced size[34–36] and to the relative large size of the Bohr exciton radius in SnO_2 (4 nm), which determines the onset of the quantum confinement regime[37]. To put the band-gap energy and in relation to NCs size, it was used the Brus's theoretical relation.[38]

$$E(R) = E_g + \frac{\hbar^2\pi^2}{2\mu_e R^2} - \frac{1.8e^2}{\varepsilon R}$$

where E_g is the bulk SnO_2 band gap (3.6 eV), $\hbar$ is the reduced plank constant, μ_e is the reduced electron mass (0.27m_e), e is the electron charge, ε is the dielectric constant (ε=14 for SnO_2)),) and R is the radius of NCs. For 3 nm one obtains a band-gap of 4.3 eV, which is 0.45 eV lower than the band gap obtained by the Tauc plot. This slight mismatch can be partly assign to a possible large uncertainties in the estimation of the band-gap by Tauc plot and/or to the error in the estimation of the NCs size from TEM images due to the blurred contours of the NCs caused by the residual organic matter. The quantum confinement is still visible for the thin film, suggesting that the NCs within the film do not coalesce due to the relatively low temperature used for annealing (150°C), thus, letting the film preserve its nanostructured morphology. However, the 150°C thermal treatment is sufficient to allow organic molecules (benzyl alcohol) to abandon the NCs surface and let them come into contact, which is critical to obtain an efficient electron transport and a high conductivity of the film. The very high value of the measured band gap also suggests that the nanoparticles are defect-free or have a very low defects concentration, respectively. Indeed, highly defective nanoparticles would have had a narrower band gap due to defect-like intraband transitions.[34] This finding further confirms the effectiveness of the MWNASG method for growing SnO_2-NCs for the casting of SnO_2 layers. SEM image of Figure S3 shows that SnO_2-NCs film deposited on ITO substrate after drying is quite uniform but presents scattered wells probably formed during the fast evaporation of the solvent. AFM image of the SnO_2-NCs evidences even better the holes observed by SEM, (see Figure S4). However, given the relatively low value of the root mean square roughness R_q = 7.04 nm found, the surface roughness appears to be still modest. The appearance of indium signal in the XPS spectrum may lead to think that SnO_2 layer has pinholes. This cannot be excluded given the holes observed in SEM and AFM images. However, considering that the XPS probing depth is about 10 nm and given the fact that the thickness of SnO_2 ETL is in that range as well, it is highly probable that XPS is probing the ITO underneath. Moreover, the high efficiency of the devices brings to exclude the presence of a large number of pinholes in the film, which would have a serious detrimental effect on cells efficiency, especially on the shunt resistance and fill factor, which is not observed. The electron mobility of the SnO_2-NCs film was investigated by space charged limited current (SCLS) method as reported in Figure S5. By fitting the Child's regime with the Mott-Gurney equation, a mobility (μ) in the order of 10^{-5} $cm^2V^{-1}s^{-1}$ was measured (see Table S1). This value of μ is lower than the value measured for mesoporous SnO_2[22], yet, it is three orders of magnitude higher than μ of amorphous SnO_2 film obtained by chemical bath deposition.[33] Figure 6a shows the J-V curve of the best performing device obtained with 3 nm SnO_2-NCs ETL, wherein the PCE is 14.2 % with a V_{OC} of 1.01 V, J_{SC} of 21.24 mA/cm^{-2}, and FF of 65.9 %. A statistic on 40 devices, evidences that the average efficiency is of 12.7 % with a respective standard deviation of 0.88 %. An histogram of the devices efficiency is given in Figure S6. For comparison, Figure S7 shows the J-V curve of the best performing $MAPbI_3$/TiO_2-NCs reference device, where the TiO_2 layer is deposited without adding the binding agent $Ti(acac)_2(^iPrO)_2$. Clearly, the performance is considerably inferior compared to $MAPbI_3$/SnO_2-NCs devices, for which also no binding agent was added. This comparison further highlights the quality of SnO_2-NCs as building blocks for ETL in organo-halide perovskite solar cells. The corresponding external quantum efficiency (EQE) spectrum is plotted in Figure 6b. The EQE is barely constant all over the spectrum but it oscillates after 650 nm probably due to light interference in the $MAPbI_3$ film which is only 250 nm thick. The cut-off wavelength of the top-performing SnO_2 ETL-based organo-halide perovskite solar cells is around 350 nm, which lies at significantly lower wavelengths than TiO_2-based devices (410 nm).[21,29] This is clearly one of the advantages of ultra-small size SnO_2-NCs-based ETL since the high transparency in the UV range significantly enhances the photo-current density of SnO_2-based device (21.2 mA/cm^{-2}) compared to its TiO_2-based reference device (15.8 mA/cm^{-2}).

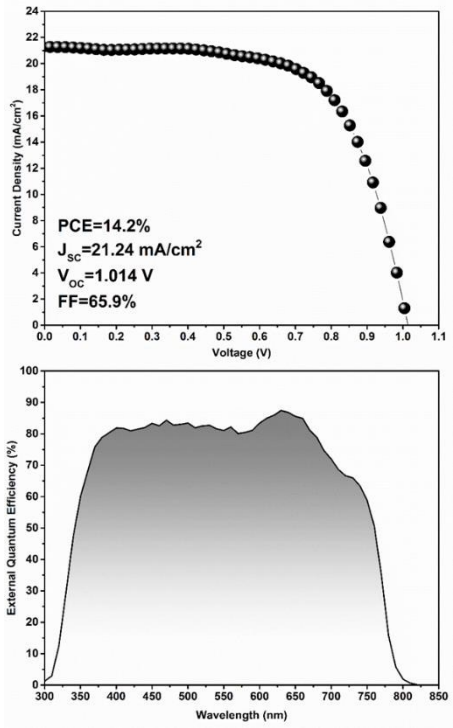

Figure 6: (a) J-V characteristic and (b) EQE spectra of the champion photovoltaic device based on SnO_2-NCs as ETL

Conclusions

In conclusion, we have successfully demonstrated a facile low-temperature solution-based preparation of tin (IV) oxide ETL starting from microwave-assisted non-aqueous synthesized SnO_2-NCs. Highly crystalline NCs were prepared in two average sizes just by adjusting the reaction time. The smallest SnO_2-NCs show a strong quantum confinement effect, even when they are cast as a thin film, which is evidenced by the larger band gap of SnO_2-NCs compared to bulk SnO_2. This results in decreased parasitic absorption and deeper work function of the SnO_2-NCs film, facilitating photo-generated electrons injection from the halide perovskite to the SnO_2 ETL. As-synthesized SnO_2-NCs were used as starting material for ETL in organo-halide-perovskite solar cells obtaining a PCE of 14.2%. As a future perspective, ultra-small sized SnO_2-NCs could be used as an efficient ETL for organic and quantum dot-based photovoltaic devices. They are also particularly attractive for perovskite/silicon tandem solar cells due to their high transparency and the low processing temperature that they require.

References

1 A. Kojima, K. Teshima, Y. Shirai and T. Miyasaka, *J. Am. Chem. Soc.*, 2009, **131**, 6050–6051.

2 2015.

3 L. Etgar, P. Gao, Z. Xue, Q. Peng, A. K. Chandiran, B. Liu, M. K. Nazeeruddin and M. Grätzel, *J. Am. Chem. Soc.*, 2012, **134**, 17396–17399.

4 H.-S. Kim, C.-R. Lee, J.-H. Im, K.-B. Lee, T. Moehl, A. Marchioro, S.-J. Moon, R. Humphry-Baker, J.-H. Yum, J. E. Moser, M. Grätzel and N.-G. Park, *Sci. Rep.*, 2012, **2**, 591.

5 D. Liu and T. L. Kelly, *Nat. Photonics*, 2013, 8, 133–138.

6 J. Liu, C. Gao, L. Luo, Q. Ye, X. He, L. Ouyang, X. Guo, D. Zhuang, C. Liao, J. Mei and W. Lau, *J. Mater. Chem. A*, 2015, **3**, 11750–11755.

7 L. S. Oh, D. H. Kim, J.-W. A. Lee, S. S. Shin, J.-W. A. Lee, I. J. Park, M. J. Ko, N.-G. Park, S. G. Pyo, K. S. Hong and J. Y. Kim, *J. Phys. Chem. C*, 2014, **118**, 140926143338002–140926143338002.

8 K. Wojciechowski, M. Saliba, T. Leijtens, A. Abate and H. J. Snaith, *Energy Environ. Sci.*, 2014, **7**, 1142–1147.

9 J. Yang, B. D. Siempelkamp, E. Mosconi, F. De Angelis and T. L. Kelly, *Chem. Mater.*, 2015, 150529083734008.

10 L. Wang, W. Fu, Z. Gu, C. Fan, X. Yang, H. Li and H. Chen, *J. Mater. Chem. C*, 2014, **2**, 9087–9090.

11 P. Qin, S. Paek, M. I. Dar, N. Pellet, J. Ko, M. Grätzel and M. K. Nazeeruddin, *J. Am. Chem. Soc.*, 2014, **136**, 8516–8519.

12 K. Do, H. Choi, K. Lim, H. Jo, J. W. Cho, M. K. Nazeeruddin, J. Ko, M. Grätzel, S. I. Seok, X. Shi, Q. Fang, S. Qian, Q. Meng and X. Li, *Chem. Commun.*, 2014, **50**, 10971.

13 K. Wang, Y. Shi, Q. Dong, Y. Li, S. Wang, X. Yu, M. Wu and T. Ma, *J. Phys. Chem. Lett.*, 2015, **6**, 755–759.

14 X. Yin, P. Chen, M. Que, Y. Xing, W. Que, C. Niu and J. Shao, *ACS Nano*, 2016, **10**, 3630–3636.

15 J. A. Christians, R. C. M. Fung and P. V. Kamat, *J. Am. Chem. Soc.*, 2014, **136**, 758–764.

16 S. Ye, W. Sun, Y. Li, W. Yan, H. Peng, Z. Bian, Z. Liu and C. Huang, *Nano Lett.*, 2015, **15**, 3723–3728.

17 Y. Xue, Y. Wu and Y. Li, *J. Power Sources*, 2017, **344**, 160–169.

18 H. Sun, X. Hou, Q. Wei, H. Liu, K. Yang, W. Wang, Q. An and Y. Rong, *Chem. Commun.*, 2016, **52**, 8099–8102.

19 A. El Labban, H. Chen, M. Kirkus, J. Barbe, S. Del Gobbo, M. Neophytou, I. McCulloch and J. Eid, *Adv. Energy Mater.*, 2016, **6**, 1502101.

20 B. O'Regan and M. Grätzel, *Nature*, 1991, **353**, 737–740.

21 H. Zhou, Q. Chen, G. Li, S. Luo, T. -b. Song, H.-S. Duan, Z. Hong, J. You, Y. Liu and Y. Yang, *Science (80-.).*, 2014, **345**, 542–546.

22 P. Tiwana, P. Docampo, M. B. Johnston, H. J. Snaith and L. M. Herz, *ACS Nano*, 2011, **5**, 5158–5166.

23 W. Ke, G. Fang, Q. Liu, L. Xiong, P. Qin, H. Tao, J. Wang, H. Lei, B. Li, J. Wan, G. Yang and Y. Yan, *J. Am. Chem. Soc.*, 2015, **137**, 6730–6733.

24 J. Song, E. Zheng, J. Bian, X.-F. Wang, W. Tian, Y. Sanehira and T. Miyasaka, *J. Mater. Chem. A*, 2015, **3**, 10837–10844.

25 H.-S. Rao, B.-X. Chen, W.-G. Li, Y.-F. Xu, H.-Y. Chen, D.-B. Kuang and C.-Y. Su, *Adv. Funct. Mater.*, 2015, **25**, 7200–

7207.

26 Y. Li, J. Zhu, Y. Huang, F. Liu, M. Lv, S. H. Chen, L. H. Hu, J. W. Tang, J. X. Yao and S. Y. Dai, *Rsc Adv.*, 2015, **5**, 28424–28429.

27 J. P. C. Baena, L. Steier, W. Tress, M. Saliba, S. Neutzner, T. Matsui, F. Giordano, T. J. Jacobsson, A. R. S. Kandada, S. M. Zakeeruddin, A. Petrozza, A. Abate, M. K. Nazeeruddin, M. Grätzel and A. Hagfeldt, *Energy Environ. Sci.*, 2015, **8**, 2928–2934.

28 Q. Jiang, L. Zhang, H. Wang, X. Yang, J. Meng, H. Liu, Z. Yin, J. Wu, X. Zhang, J. You, A. Kojima, K. Teshima, Y. Shirai, T. Miyasaka, H. S. Kim, M. M. Lee, J. Teuscher, T. Miyasaka, T. N. Murakami, H. J. Snaith, N. J. Jeon, J. H. Noh, Y. C. Kim, W. S. Yang, S. Ryu, S. I. Seok, S. D. Stranks, G. Xing, M. Liu, M. B. Johnston, H. J. Snaith, H. Zhou, J. Y. Jeng, J. You, L. Meng, J. You, T. F. Guo, Y. Yang, W. Tress, Z. Xiao, Y. Zhao, K. Wojciechowski, K. Wojciechowski, Y. W. Li, G. Xing, S. D. Stranks, H. J. Snaith, H. J. Snaith, C. Ducati, B. Bob, Q. Dong, J. Song, Y. Li, W. Ke, J. P. C. Baena, S. Yang, J. K. Kwak, W. Hu, Z. Xiao, S. Pang, N. J. Jeon, J. You, Q. Chen, Y. C. Kim, Z. Xiao, D. W. De Quilettes, A. G. Aberle, C. Algora, W. Chen, B. Chen, M. Yang, S. Priya, K. Zhu, Y. Shao, R. O'Hayre and H. J. Daal, *Nat. Energy*, 2016, **1**, 16177.

29 M. Liu, M. B. Johnston and H. J. Snaith, *Nature*, 2013, **501**, 395–8.

30 J. Ba, J. Polleux, M. Antonietti and M. Niederberger, *Adv. Mater.*, 2005, **17**, 2509–2512.

31 L. Luo, M. D. Rossell, D. Xie, R. Erni and M. Niederberger, *ACS Sustain. Chem. Eng.*, 2013, **1**, 152–160.

32 I. Bilecka, I. Djerdj and M. Niederberger, *Chem. Commun.*, 2008, 886–888.

33 S. D. G. Jérémy Barbé, Max L. Tietze, Marios Neophytou, Abdulrahman El Labban, Mutalifu Abulikemu, Wan Yue, Murali Banavoth, Omar F. Mohammed, Iain McCulloch, Aram Amassian, *ACS Appl. Mater. Interfaces*, 2017.

34 V. B. Kamble and A. M. Umarji, *AIP Adv.*, 2013, **3**.

35 E. J. H. Lee, C. Ribeiro, T. R. Giraldi, E. Longo, E. R. Leite and J. a. Varela, *Appl. Phys. Lett.*, 2004, **84**, 1745.

36 H.-X. Deng, S.-S. Li and J. Li, *J. Phys. Chem. C*, 2010, **114**, 4841–4845.

37 M. B. Sahana, C. Sudakar, A. Dixit, J. S. Thakur, R. Naik and V. M. Naik, *Acta Mater.*, 2012, **60**, 1072–1078.

38 L. E. Brus, *J. Chem. Phys.*, 1984, **80**, 4403–4409.